Chapter 7

Additional research into novel whispering-gallery devices

7.1 Introduction

Whispering-gallery devices (e.g., microtoroid) have additional applications aside from those previously discussed, and countless more to be discovered, due to their unique ability to confine light for long periods of time in small mode volumes. For example, the author has investigated spiral waveguides for real-time optical delay, in which WGM propagate significant distances within a small surface area. Also, the author is investigating a dual-doped Cr,Yb:SiO_2 pulsed laser design based on the microtoroid geometry. The Quantum Optics group at Caltech, led by Professor Jeff Kimble, has conducted research on cavity-atom interactions using microtoroids fabricated by the author [30, 31].

7.2 Spiral delay line

The author has conducted research on a novel on-chip optical delay line based on whispering-gallery propagation of light through a spiral waveguide. Optical delay elements are needed for all-optical packet switching for communications [112], and also for laser-based radar systems [113]. Currently, state-of-the-art optical delay lines are made from coils of optical fiber in a large package, whose fabrication is time consuming and expensive. Therefore, there is significant interest today in an on-chip lithographically fabricated real-time optical delay line with attenuation similar to optical fiber. Optical lithography offers precise control over waveguide dimensions, and allows parallel fabrication of many delay-lines with precise and possibly different time delay on the same silicon wafer.

The new optical delay line developed by the author combines two waveguide technologies. First, the waveguide is defined by two Archimedean spirals connected in the center for long-delay in a small area. A stereo-microscope image of the largest silica-on-silicon spiral waveguide the author fabricated is shown in Figure 7.1. The physical length of this spiral is 1.4 m, and the limits of the spiral fit within an area of less than 0.4 cm^2. The spiral geometry is well-recognized as an efficient way to pack long delay into a small space. A GaAs spiral waveguide for optical delay [114] and

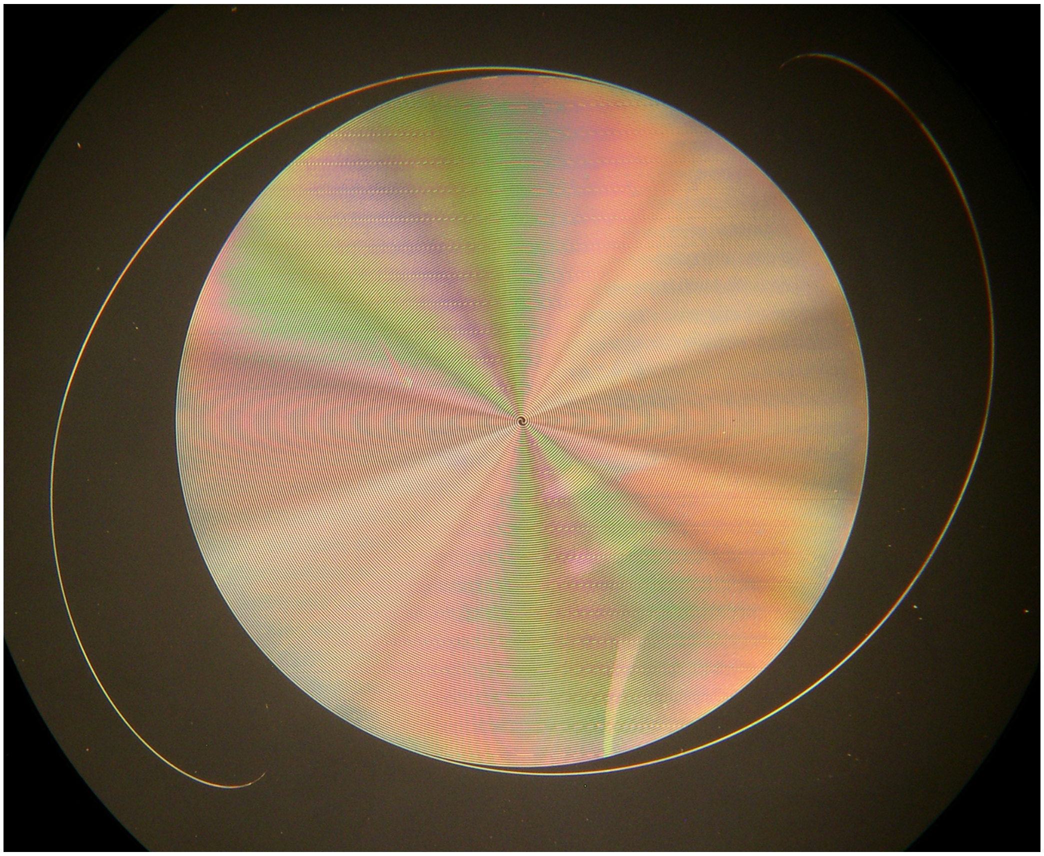

Figure 7.1. Stereo-microscope image of a large silica spiral waveguide with 1.4 m total propagation length defined within < 0.4 cm^2 area

an Er-doped Al_2O_3 spiral waveguide amplifier [115] have been reported. The largest source of loss in a twin-spiral waveguide is the center region, where the WGM must transition from clockwise to counterclockwise propagation. Here, the optical wave must move across the waveguide and switch sides, without exciting higher order modes. The author has conducted detailed simulations of the center "hand-off" region to optimize the transmission, as will be discussed in Section 7.2.1.1.

A second key technology that will enable low-loss propagation in the spiral waveguide is the silica wedge cross-section developed for UHQ silica microdisks [116]. While microtoroids can have higher Q than microdisks due to their nearly atomic smooth surface, the cavity diameter change during reflow makes integrated waveguide coupling to microtoroids difficult. Silica microdisks can be fashioned with a bevelled edge (or wedge) by control of the wet-etch chemistry. To form a wedge, the normal adhesion promoter is not applied before photoresist deposition, which allows the hydrofluoric acid to undercut the photoresist and form a low-angle bevel during the BOE etch step. An SEM micrograph of a wedged microdisk resonator is presented in Figure 7.2.

The bevel confines the whispering-gallery-mode and pushes it deep into the silica, away from lithographic roughness at the extreme edge. In this way, surface scattering is reduced and the

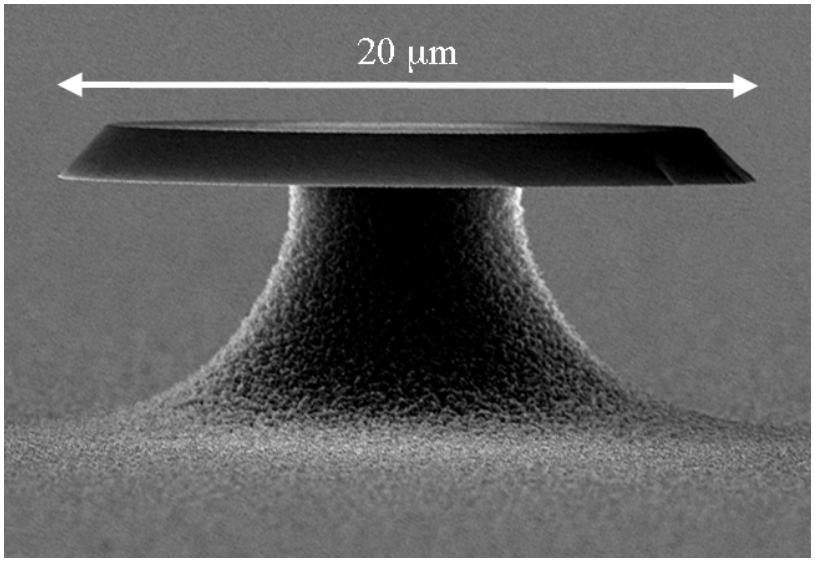

Figure 7.2. SEM image of a 20 μm diameter silica microdisk with wedge feature to confine the WGM away from surface roughness visible at the knife edge

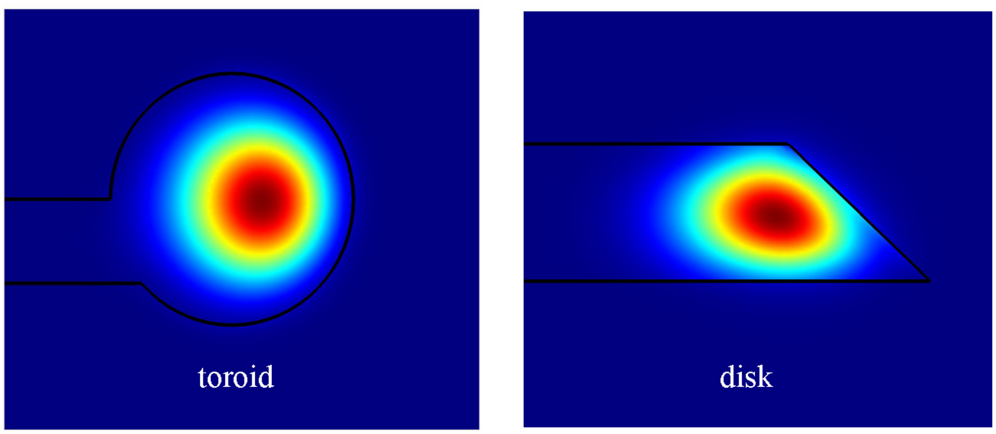

Figure 7.3. Comparison image of the WGM field pattern for a microtoroid (left) and a wedged microdisk (right). The WGM is confined further away from the extreme edge in the microdisk.

microdisk cavity Q increases. The mode confinement caused by the bevel silica surface is illustrated in Figure 7.3.

To illustrate the benefit of the silica bevel, Kippenberg demonstrated a wedged microdisk with Q as high as 6×10^7 [116], a significant improvement in Q over the normal microdisk Q (1×10^6). The effective waveguide loss for a microdisk resonator with $Q = 6 \times 10^7$ is 4×10^{-3} dB/cm, compared to silica fiber's intrinsic loss of 2×10^{-6} dB/cm. Clearly, there is room for improvement in wedged WGM propagation loss in silica, which can be achieve with lower index contrast cladding and higher purity silica deposition by flame hydrolysis. But, assuming the worst case scenario in which the wedged waveguide loss is not reduced, a 3 m long spiral can be fabricated in a 1 cm^2 area with only 1 dB of transmission loss.

7.2.1 Spiral waveguide design

A spiral with any number of total turns and turn pitch can be designed with a Matlab program the author wrote. The spiral consists of two Archimedean spiral arms, which are joined in the center by a custom transition region where the optical wave reverses circulation direction. Archimedean spirals were chosen for their smoothness and simplicity. The functional equation that generates an Archimedean spiral is easily written in polar coordinates.

$$r(\theta) = a \pm b\theta \tag{7.1}$$

Parameter a controls the starting position of the spiral by rotating the spiral around the origin, and parameter b determines the distance between successive turnings. One arm of an Archimedean spiral with three complete rotations is shown in Figure 7.4.

If two Archimedean spiral arms (one positive, one negative) are simply joined by brute force in the center, then the waveguide that results will have significant loss due to the severe bending. Alternatively, a custom center hand-off region that connects the two opposite arms smoothly is designed in Matlab.

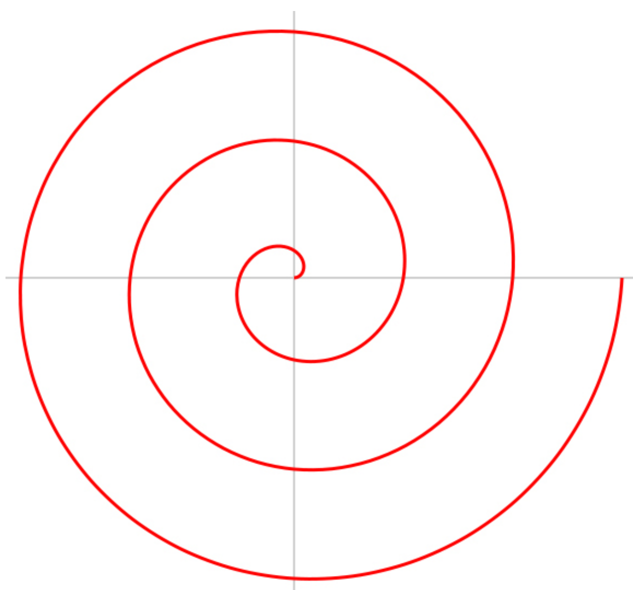

Figure 7.4. Single Archimedean spiral with three rotations; two arms are joined to form the complete spiral geometry of this work.

7.2.1.1 Spiral center transition

The center transition region (hand-off) must guide the light propagating in the positive spiral arm (clockwise rotation), into the negative spiral arm where the light will propagate in the counterclockwise direction. This transition region is most simply implemented in a smooth s-shaped curve. But, the curvature of the s-bend can follow any type of function, for instance sinusoidal or circular to name just two. The optimum shape will be determined by final transmission through the hand-off region.

In order to quantify the transmission loss through different s-bend designs, the author conducted simulations of the transmission with the commercial BeamPROP software (RSoft). BeamPROP is a waveguide design tool based on the Beam Propagation Method (BPM), and is capable of performing 3D simulations. Applied to the spiral waveguide, the simulation calculates the percentage of power that is transmitted from a single-mode whispering-gallery mode in one arm into the symmetric single mode in the arm. First, the lowest-order WGM field distributions of both positive and negative curvature are determined with the FEM solver. The geometric cross-section of the spiral waveguide is a trapezoid shape, shown with the fundamental WGMs for positive and negative curvature in Figure 7.5. The bottom width of the waveguide is 8 μm and the bevel angle is 45°.

Then, the positive curvature end of the s-bend waveguide is excited with the exact field distribution of an incident optical field from the positive spiral arm. Next, the optical field is propagated through the s-bend curve being studied. At the output of the negative curvature end of the s-curve, an overlap integral is computed of the optical field that passes through the s-bend and the single-mode WGM field that will propagate through the negative arm of the spiral. The value of this

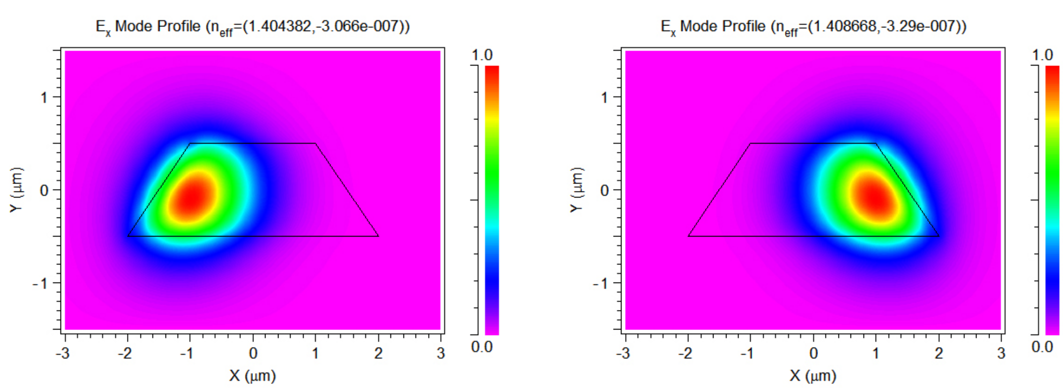

Figure 7.5. Field distributions of negative (left) and positive (right) spiral spatial modes. The field profiles are calculated by FEM, and show the effect of waveguide curvature on the mode position in the cross-section view.

integral is the fraction of incident power that actually couples from a single mode in the positive spiral arm into the single mode of the negative arm after passing through the center transition region.

Circular s-curves were studied through beam propagation simulation as described above, since they could be easily implemented into the software. The s-curve consists of two quarter circles (20 μm radius of curvature) with opposite curvature, connected at their ends. For optimum transmission, the waveguide should be close to single mode in the center. Also, the center region must be undercut completely, not supported by a silicon wall, otherwise the optical radiation traveling in silica will leak out into the silicon (higher refractive index). But, the main spiral cannot be made with single-mode width, since the spiral must be kept flat in one plane by the silicon support. Therefore, a symmetric linear taper of the waveguide width from 4 to 2 μm is included on both sides of the s-bend design. At the ends of the s-bend, the waveguide cross-section dimensions are identical to the trapezoid shape used for the FEM solver. But, the waveguide tapers down to a smaller width in the center for increased transmission.

Initially, simulations of the s-bend transmission were conducted with no horizontal offset at the center of the quarter circles. However, with no offset, the maximum transmission was only 61%. Previous work on s-bends in optical modulators determined that a horizontal offset reduces transmission losses in bent waveguides [117]. A physical horizontal offset was inserted between the two quarter circles, and its value was optimized for highest transmission through the transition region. For an s-curve with dimensions of $R = 20\ \mu$, $2 \leq w \leq 4$, and thickness $t = 2\ \mu$m, the optimum offset for single-mode transmission of 1550 nm light is $\Delta x = 1.8\ \mu$m. The final transmission through the s-bend waveguide with these parameters is 88%. Figure 7.6 is a plot of the s-bend design showing the waveguide width taper and horizontal offset in the center. Future research into other transitional functions and parameters will increase the transmission. Perhaps a true single-mode center hand-off can be designed and fabricated for higher transmission. The current design presented did not have a single-mode waveguide element, instead it relied on offset and tapering to prevent the single WGM from coupling into other modes.

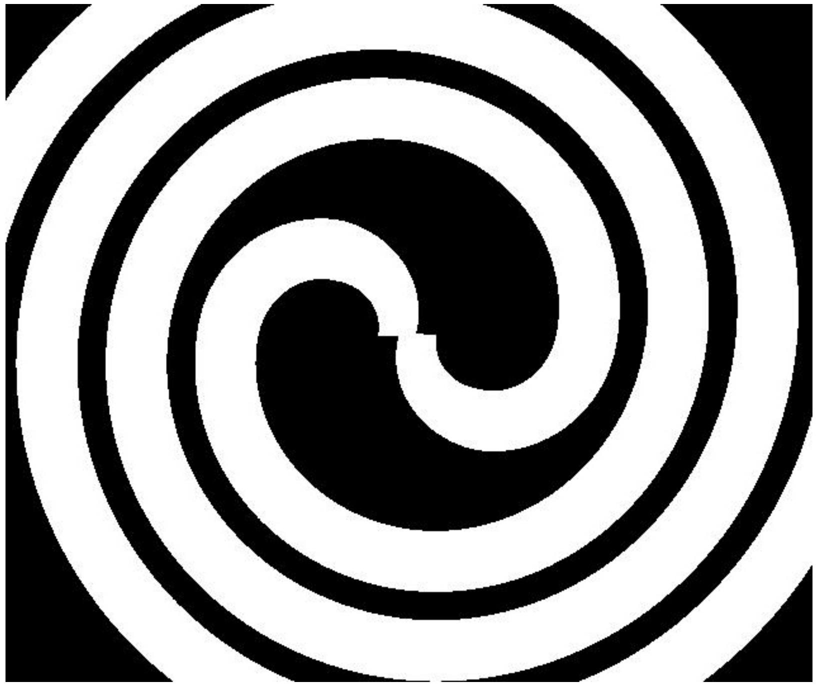

Figure 7.6. Plot of the center s-bend design for high transmission in a spiral waveguide

7.2.2 Spiral waveguide fabrication

Several different spiral waveguides are fabricated to demonstrate the device and measure its transmission of light. Standard photolithography and etching techniques are utilized, similar to the fabrication of microtoroids. First, a layer of photoresist is spin coated onto a silicon wafer with 2 μm thermal oxide on top, using HMDS to increase the adhesion and prevent over etching of the narrow hand-off region in the spiral center. The spiral pattern designed using Matlab and BeamPROP is transferred into the photoresist with an industry grade wafer stepper, providing the highest resolution possible in our facilities. After the exposed photoresist is removed by developer, the spiral pattern is transferred into the fused silica layer by BOE wet etch. The etching time is carefully controlled to produce the 45° bevel as designed, without over etching the center s-bend region. Finally, a XeF_2 dry etch completely undercuts the silica s-bend region in the spiral center, and leaves the spiral waveguide supported by thin rails of silicon. An SEM image of the center portion of one completed spiral is shown in Figure 7.7. The center hand-off region with the width tapering and center offset is visible.

The silicon wafer was cleaved directly through a spiral waveguide, revealing the sidewall bevel and cross-section of the wedged waveguide supported by silicon (Figure 7.8).

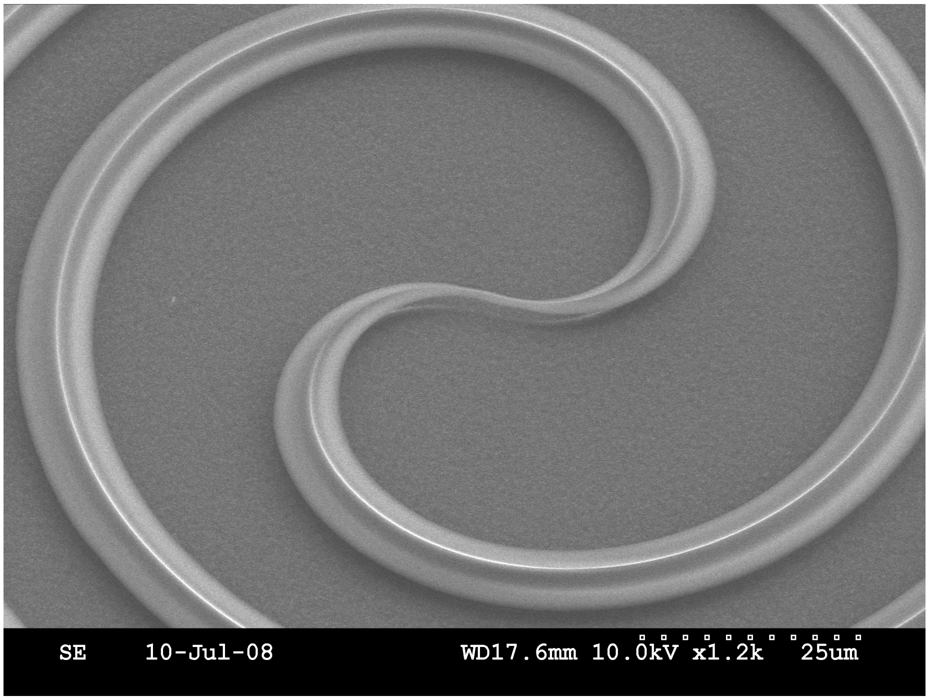

Figure 7.7. SEM image of the center portion of one completed silica on silicon spiral waveguide. Notice that the center transition region of the spiral is completely undercut.

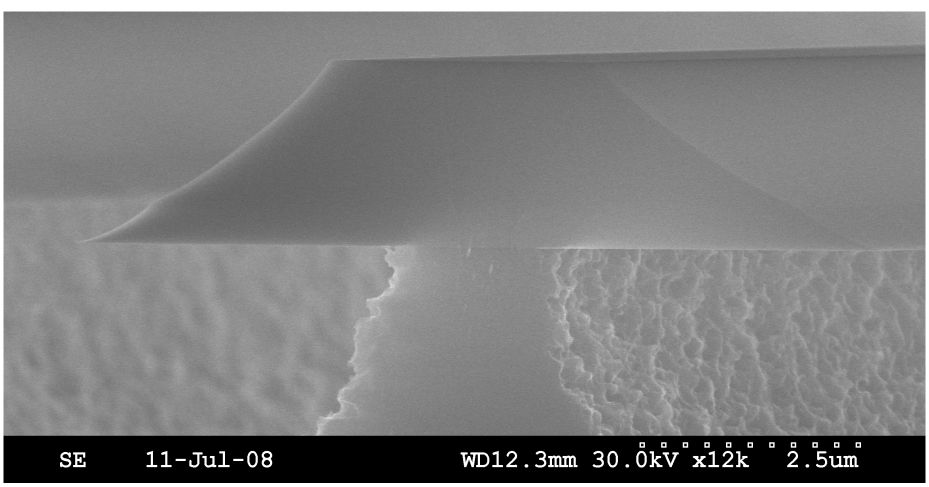

Figure 7.8. SEM image of a cleaved spiral showing the waveguide cross-section with sidewall bevel and silicon support

7.2.3 Spiral waveguide measurement

In addition to the larger spirals fabricated for physical demonstration (see Figure 7.1), smaller single-turn spirals are made for measurement of the transmission loss of the s-bend hand-off region. The largest source of loss at this stage is believed to be due to the center region. In order to perform accurate insertion loss measurements of the spiral waveguide, two fiber tapers are pulled simultaneously. A dual-fiber taper drawing system is constructed that pulls two tapers over a single hydrogen flame, similar to that used for dual taper testing of a microtoroid four-port coupler [107]. To make two quasi-identical tapers, the flame location and hydrogen gas flow are carefully optimized. After significant trial and error, dual tapers separated by 0.5 mm are fabricated with high transmission and nearly identical diameters.

The spiral waveguide is elevated until it is in close contact with both tapers, the spiral waveguide outer diameter is 100 μm. The spiral position is adjusted using nanopositioning stages, one taper is fixed in place, and the second taper is controlled by a probe attached to the taper. To make an accurate measurement of the transmission through the short spiral, the transmission of each taper is recorded. The input fiber is aligned to the input arm of the spiral at the outside of the bevel. This spiral is moved until maximum extinction is achieved, indicating maximum power transfer into the spiral waveguide. The output taper is precisely moved until output radiation is measured at the end of the fiber. The output fiber radiation is the light that couples into the spiral input arm, propagates through the spiral (including the center hand-off region), and couples out into the output fiber. A microscope image of the short spiral and two fiber tapers is shown in Figure 7.9. The ratio of output power to input power is computed, and then adjusted for taper losses. This final value is the percentage of light that is coupled through the spiral waveguide, and contains any taper-spiral coupling losses. The highest transmission measured for the first short spiral is 4 %, indicating that significant loss accumulates either in the hand-off region or taper coupling, or both.

In the future, numerous different short spirals will be tested to determine the best s-bend design, quantified by the spiral transmission. Then, larger spirals with quantified lengths and identical center regions will be tested to determine the transmission loss of the spiral arms themselves, independent of the center transition region.

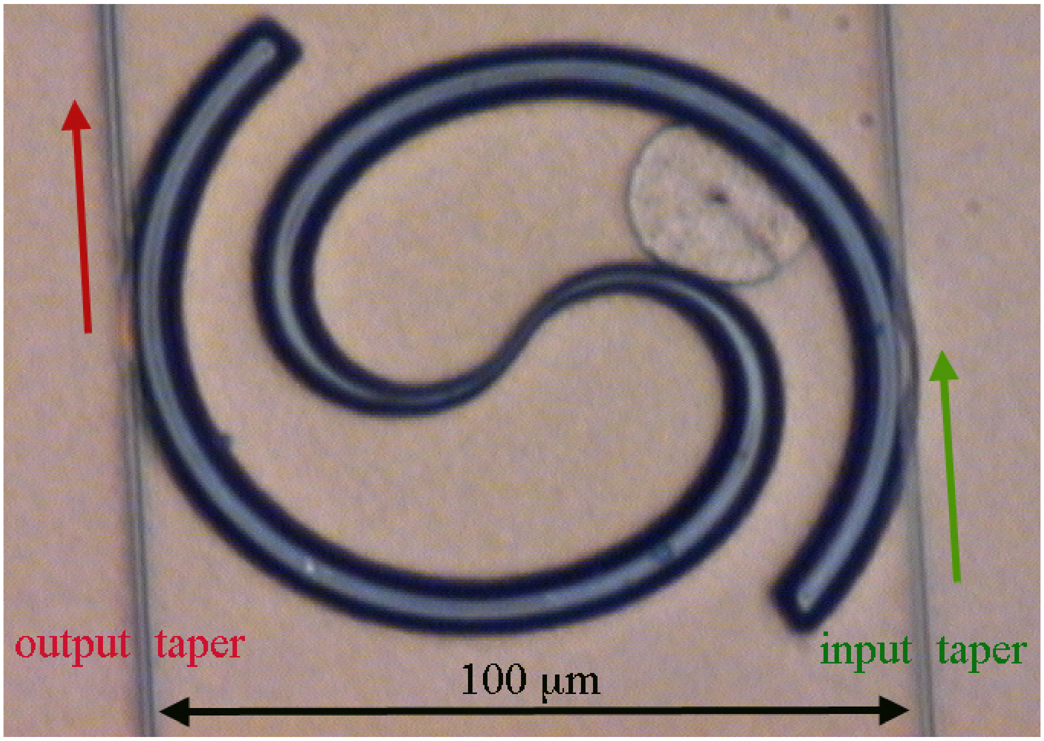

Figure 7.9. Top view of the one-turn two arm spiral with dual fiber taper coupling for transmission measurement. The outer diameter of the spiral is 100 μm.

7.3 Short-pulse microcavity laser

The Yb:SiO_2 microtoroid sol-gel lasers presented in Chapters 3 and 4 normally operated with continuous output power. However, unstable 100 ns duration pulses were observed in higher ytterbium concentration toroid lasers as discussed in Section 3.6.4. A stable short-pulse microcavity laser has never been demonstrated, and is an interesting field of research.

7.3.1 Laser concept

The author has developed a new short-pulse microcavity laser concept made possible by flexible doping of solgel silica. The short pulse laser operates by passive Q switching in a dual doped Cr,Yb:SiO_2 microtoroid. The microtoroid laser can be easily fashioned according to the solgel fabrication method, by including chromium nitrate and ytterbium nitrate in the solution before the main chemical reaction occurs. The author gained experience in short pulse lasers with his work developing a Yb:YAG microchip laser oscillator with a Cr:YAG passive Q switch [52].

Q switched lasers produce short pulses due to repeated modulation of the cavity loss or gain. This dual doped laser receives gain from the ytterbium ions, and time-dependent loss from the chromium ions. Chromium (Cr^{4+}) ions have an intensity dependent cross-section of absorption

(σ). The ground state cross-section of chromium is $\sigma_g = 4 \times 10^{-20}$ cm^{-2}, and the excited state cross-section is $\sigma_e = 7 \times 10^{-21}$ cm^{-2}. Inside the laser microcavity, the absorption loss caused by Cr^{4+} ions in the ground state prevent laser emission at low intracavity intensities. However, the constant-power pump light linearly increases the stored energy in the ytterbium ions, and hence the intracavity intensity. Once the intensity reaches a threshold value, the chromium ions transition from the ground to excited state, and their absorption loss drops. At this point, the cavity gain (from Yb) is greater than the cavity loss (from Cr, coupling, scattering, etc.) and a giant pulse is emitted from the microtoroid cavity laser as the ytterbium ions coherently decay by stimulated laser emission.

7.3.2 Pulsed laser modeling

A numerical model of the short-pulse Cr,Yb:SiO_2 laser was implemented by the author in Matlab to research the design considerations and predict the laser performance. This laser model builds on the short-pulse laser model developed by Dong et al. for Cr,Yb:YAG microdisk lasers [118]. The initial (N_i), threshold (N_t), and final (N_f) ytterbium population inversion densities are calculated by solving the laser rate equations. Then, the laser pulse energy (E_p), peak pulse power (P_{peak}), and pulse duration (τ_p) are computed as,

$$\begin{aligned} P_{th} &= \frac{N_i A l h\nu}{\tau_{Yb}} \\ E_p &= \frac{h\nu A}{4\sigma} ln\left(\frac{1}{R}\right) ln\left(\frac{N_i}{N_f}\right) \\ P_{peak} &= \frac{h\nu A l}{2t_r} ln\left(\frac{1}{R}\right)\left[N_i - N_{th} - N_{th} ln\left(\frac{N_i}{N_f}\right)\right] \\ \tau_p &\approx \frac{E_p}{P_{peak}} \end{aligned} \tag{7.2}$$

where A is the laser cavity mode area, $R = 1 - T$ is the round trip total cavity loss, t_r is the cavity round trip time, and σ is the stimulated emissions cross section of ytterbium.

Extensive simulations were conducted to elucidate the performance of the Cr,Yb doped silica microtoroid laser. The final configuration under consideration is a microtoroid cavity with 50 μm diameter, 5×10^{18} cm^{-3} Cr^{4+} concentration, and 5×10^{19} cm^{-3} Yb^{3+} concentration. The pulsed laser model just described predicts that the Q switched microcavity laser will generate a pulse train with 1 ns pulse duration, 100 pJ pulse energy, and 1 MW/cm^2 peak intensity. This laser is also expected to have a pump threshold of 1 μW, easily reached with existing tunable semiconductor diode lasers. Therefore, it is expected that such a chromium and ytterbium doped silica microtoroid laser, fabricated by sol-gel, will produce stable laser pulses.

The microcavity laser pulse duration (τ_p) is inversely dependent on the chromium concentration (N_{Cr}) as shown in Figure 7.10. Laser pulses as narrow as 10 ps can be generated by increasing

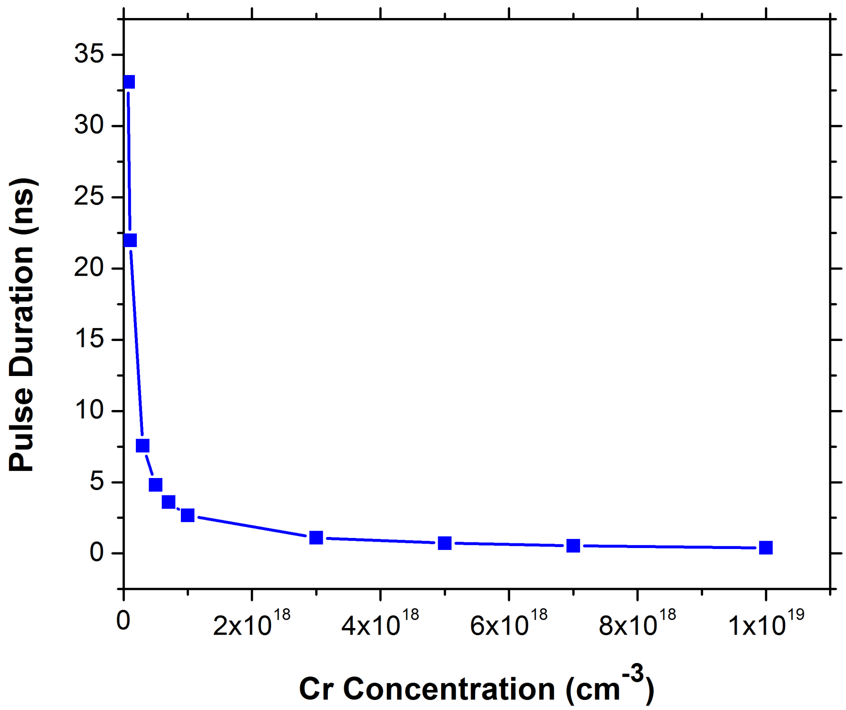

Figure 7.10. Plot of the Cr,Yb:SIO_2 microtoroid pulse duration as a function of Cr^{4+} concentration. This curve was generated for a fixed ytterbium concentration of $N_{Yb} = 5 \times 10^{19}$ cm^{-3} and 50 μm toroid diameter.

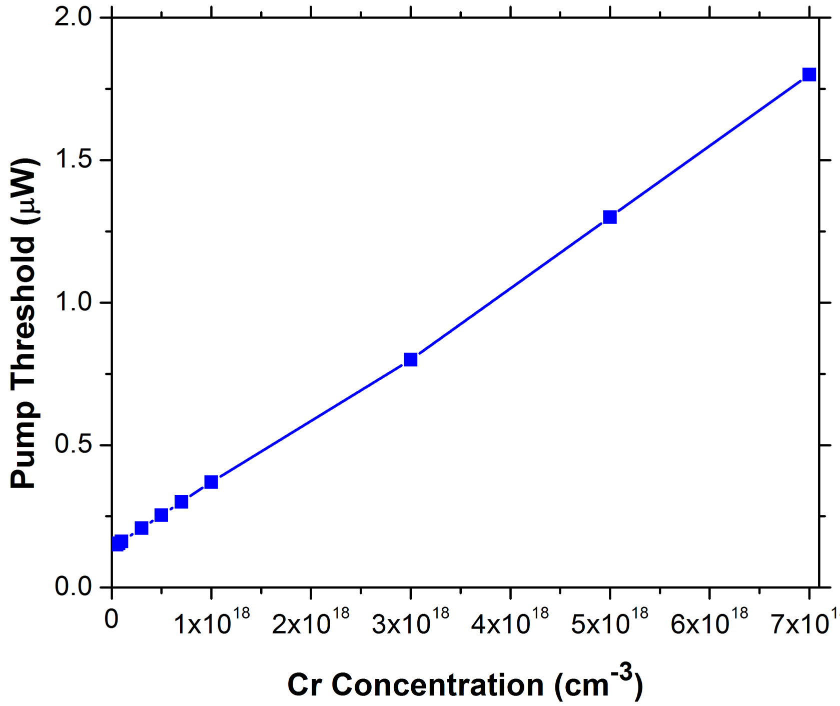

Figure 7.11. Plot of the pulsed laser threshold as a function of Cr^{4+} concentration for a 50 μm toroid

the chromium concentration, but will require higher pump power. Simulation also demonstrates in Figure 7.11 the linear dependence of laser pump threshold on chromium concentration.

A short-pulse laser, like the one designed here, will offer new areas of scientific research in microcavities. For instance, a pulsed laser can be used as a light source for on-chip optical communication. Also, the laser pulse train is very sensitive to any sources of loss, and may find application as a particle or biological sensor. Now, it is up to future research to experimentally demonstrate this novel passively Q switched laser and apply it to new problems.

7.4 Microtoroids for atom cavity experiments

The author collaborated with the Kimble research group at Caltech, by fabricating UHQ and ultralow mode volume microtoroids for their cavity quantum electrodynamics (cQED) experiments. Utilizing these toroids, a novel photon turnstile and a high-efficiency single-photon router were demonstrated. Cavity QED is the study of the interaction between light confined in a cavity and atoms or other particles, for situations when the quantum nature of photons is evident. In principle, cQED research could be used to construct a quantum computer.

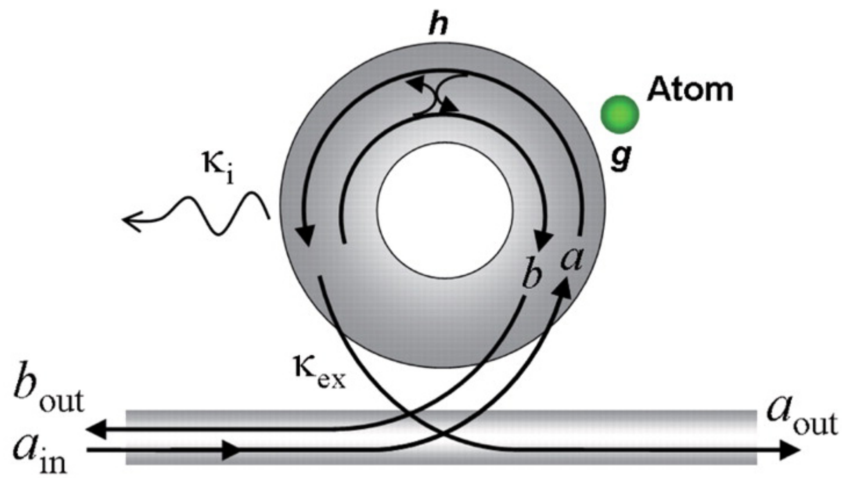

Figure 7.12. Schematic of microtoroidal resonator and fiber taper coupler. A cesium atom interacts at rate g with the evanescent fields of two cavity modes (a,b), which are coupled by scattering.

7.4.1 Cavity quantum electrodynamics

The strong coupling rate, g, between an electromagnetic field and an atomic system can be defined in terms of the cavity and atom parameters.

$$g = \gamma_{\perp}|E|\sqrt{V_a/V_m} \tag{7.3}$$

Here, $\gamma_{\perp}$ is the transverse atomic dipole transition rate, $|E|$ is the cavity's electric field strength at the atom location, V_a is the atom interaction volume, and V_m is the cavity mode volume. Strong coupling between a microtoroid and a cesium atom was shown by Aoki[17]. To satisfy the strong coupling condition, the rate of atom to cavity coupling must exceed all other dissipation mechanisms, therefore $g >> (\kappa, \gamma_{\perp}, T^{-1})$. The toroid cavity decay is defined as $\kappa = \frac{\pi c}{\lambda Q}$. Also, T is the length of time that the cavity and atom are strongly coupled.

Since photons have small intracoupling cross sections, a material system must be used for their interactions. Still, typical materials produce photon to photon coupling rates that are orders of magnitude too small for significant dynamics with photon pairs. But, in cavity quantum electrodynamics (cQED), strong interactions between single photons of light and matter have been demonstrated, including single atoms coupled to optical resonators, and quantum dots paired with photonic bandgap cavities.

Photon blockade is observed, in which photon transport is regulated dynamically by the conditional state of one intracavity atom. As illustrated in Figure 7.12, an atom interacting with the fields of a microtoroidal resonator regulates the photon statistics of light transmitted and reflected by the resonator [17]. This control is made possible by the interference of the directly transmitted optical field, the intracavity field, and the polarization field radiated by the atom. The quantum emission of the single atom provides nonlinearity, required for the turnstile behavior. The presence of a photon in the forward transmission causes any subsequent photons to be directed back towards the pump source.

The observation of photon anti-bunching relied on measurements of photon correlations based on the normalized intensity correlation function $g_F^{(2)}(\tau)$ for the forward-propagating transmitted light [119]. The incident field has $g_F^{(2)}(\tau) = 1$, corresponding to a Poisson distribution for photon number independent of time delay τ. An ideal photon turnstile would achieve $g_F^{(2)}(0) = 0$ in correspondence to the state of a single photon. More generally, $g_F^{(2)}(0) < 1$ represents a nonclassical effect with the variance in photon number reduced below that of the incident field. The observation $g_F^{(2)}(0) < g_F^{(2)}(\tau)$ represents photon anti-bunching−photons are transported one by one through the turnstile.

7.4.2 Experimental details

In the photon turnstile experiment, individual cesium atoms are dropped vertically through the evanescent field of the resonator. The author fabricated the toroidal resonator from SiO_2 on a silicon chip [10], had major diameter $D \approx 25\,\mu$m and minor diameter $d \approx 6\,\mu$m. The microtoroid and single-mode fiber taper waveguide are located inside an ultrahigh vacuum chamber.

With the taper and toroid in critical coupling, the transmitted power is sent to two single-photon counters, with the outputs from these detectors being time-stamped and stored for time bins for each time value. Then, the cross correlation is calculated from the time-stamped photon counting records.

7.4.3 Demonstration of anti-bunching and sub-Poissonian statistics

The intensity correlation function exhibits clear anti-bunching and sub-Poissonian photon statistics, demonstrated by a dip in the correlation function near $t = 0$. The efficiency of single photons is measured as high as 25% during single-atom transit events. Because the toroidal resonators are lithographically fabricated with input-output coupling via optical fiber, this experiment is a key step into the quantum domain towards implementing compact atom-cavity systems.

7.4.4 High efficiency single photon routing

The author also fabricated a small diameter, 20 μm, microtoroid cavity that showed higher efficiency routing of single photons as a part of an atomic system [31]. Single photons from a coherent laser input were efficiently directed to a separate output by way of a fibercoupled microtoroidal cavity interaction with individual cesium atoms. By operating in an overcoupled regime for the input-output to a tapered fiber, this system works as a quantum router with high efficiency. Single photons are reflected back towards the input, and excess photons are transmitted, as proven by observations of photon antibunching for the reflected light. The single photons are directed to a separate output with an efficiency of $\xi \approx 0.6$.

Detection of a first photon for the reflected field forces the cesium atom into its ground state, which prevents the detection of a second photon [30, 120]. Therefore, the reflected light shows sub-Poissonian photon statistics and photon antibunching. Single photons are reflected the excess photons are transmitted into the forward field. In the future, the routing efficiency can approach $\xi > 0.999$ through use of microtoroids with smaller major diameter and higher intrinsic q factor [11, 121].

7.4.5 Fabrication of small mode volume UHQ microtoroids for cQED research

The author fabricated small-mode volume microtoroids for the atom and cavity experiments detailed above. These microtoroids have a major diameter (D) of only 25 μm. To create these small toroids, small silica microdisks, 40 μm diameter, were first made by photolithography and wet etching. The XeF_2 etch reduced the silicon pillar diameter to approximately 10 μm. Then, the microdisks were selectively reflowed using a single 100 ms duration CO_2 laser pulse. The final microtoroid major diameter is 20–25 μm, the minor diameter is 4–5 μm. The fundamental whispering-gallery mode volume, V_m, is estimated to be only 40 μm^{-3}. These small mode volume toroids can provide a very high atom-cavity coupling rate, g, due to the inverse relationship between the coupling rate and cavity mode volume (see Equation (7.3)).

7.4.6 Vacuum reflow of microtoroids for cQED

In the photon turnstile experiment, the microtoroid quality factor was modest at $Q = 3 \times 10^6$. For future work, higher Q is required to meet the strong-coupling condition and allow for more advanced quantum optics research. The author's work on vacuum reflow of microtoroids, discussed in **Chapter 5**, will produce higher quality factors, theoretically up to $Q = 1 \times 10^{10}$. The increase in the microtoroid cavity Q leads to an important reduction in the critical atom number, or the number of Cesium atoms required to affect the optical cavity [11]. In the future, microtoroid reflow and quantum optics research may be performed in a single vacuum chamber, leveraging ultra-high Q microtoroids for new research applications.

7.5 Summary

In this chapter, several additional research projects involving novel whispering-gallery devices were discussed. An on-chip, low-loss spiral waveguide for optical delay was investigated. Beam propaga-